

# Mafic Archean continental crust prohibited exhumation of orogenic UHP eclogite

Richard Palin (✉ [richard.palin@earth.ox.ac.uk](mailto:richard.palin@earth.ox.ac.uk))

University of Oxford <https://orcid.org/0000-0002-6959-0462>

James Moore

Earth Observatory of Singapore, Nanyang Technological University <https://orcid.org/0000-0001-8912-2730>

Zeming Zhang

Institute of Geology

Guangyu Huang

State Key Laboratory of Lithospheric Evolution

---

## Article

**Keywords:** UHP orogenic eclogite, Archean, subduction

**Posted Date:** March 19th, 2021

**DOI:** <https://doi.org/10.21203/rs.3.rs-127916/v1>

**License:** © ⓘ This work is licensed under a Creative Commons Attribution 4.0 International License.

[Read Full License](#)

---

1 Mafic Archean continental crust prohibited exhumation of orogenic  
2 UHP eclogite

3

4 **Richard M. Palin<sup>1</sup>, James D. P. Moore<sup>2,3</sup>, Zeming Zhang<sup>4</sup> and Guangyu Huang<sup>5</sup>**

5 *<sup>1</sup>Department of Earth Sciences, University of Oxford, Oxford, OX1 3AN, United Kingdom*

6 *<sup>2</sup>Earth Observatory of Singapore, Nanyang Technological University, Singapore*

7 *<sup>3</sup>Institute of Geophysics, SGEES, Victoria University of Wellington, Wellington, New Zealand*

8 *<sup>4</sup>Institute of Geology, Chinese Academy of Geological Sciences, Beijing 100037, China*

9 *<sup>5</sup>State Key Laboratory of Lithospheric Evolution, Institute of Geology and Geophysics, Chinese  
10 Academy of Sciences, Beijing 100029, China*

11

12 **The absence of ultrahigh pressure (UHP) orogenic eclogite in the geological record older**  
13 **than c. 0.6 Ga is problematic for evidence of subduction having begun on Earth during the**  
14 **Archean (4.0–2.5 Ga). Many eclogites in Phanerozoic and Proterozoic terranes occur as**  
15 **mafic boudins encased within low-density felsic crust, which provides positive buoyancy**  
16 **during subduction; however, recent geochemical proxy analysis shows that Archean**  
17 **continental crust was more mafic than previously thought. Here, we show via petrological**  
18 **modelling that secular change in the composition of upper continental crust (UCC) would**  
19 **make Archean continental terranes negatively buoyant in the mantle before reaching UHP**  
20 **conditions. Subducted or delaminated Archean continental crust passes a point of no**  
21 **return during metamorphism in the mantle prior to the stabilization of coesite, while**  
22 **Proterozoic and Phanerozoic terranes remain positively buoyant at these depths. UHP**  
23 **orogenic eclogite may thus readily have formed on the Archean Earth, but could not have**

24 **been exhumed, weakening arguments for a Neoproterozoic onset of subduction and plate**  
25 **tectonics. Further, isostatic balance calculations for more mafic Archean continents**  
26 **indicate that the early Earth was covered by a global ocean over 1 kilometre deep.**

27

## 28 **INTRODUCTION**

29 Eclogites are high-pressure (HP) metabasalts dominated by garnet and sodic clinopyroxene<sup>1</sup> and  
30 typically occur as xenoliths in mantle-derived magmas (Type A), boudins/lenses within felsic  
31 gneiss terranes (Type B), blocks encased within tectonic mélangé (Type C), or metamorphosed  
32 and exhumed slices of oceanic lithosphere (Type D)<sup>2</sup>. A subdivision of the eclogite facies is  
33 defined by pressure–temperature ( $P$ – $T$ ) conditions sufficient to transform quartz to coesite (~2.6–  
34 2.8 GPa at ~500–900 °C), which is termed ultrahigh pressure (UHP) metamorphism<sup>3</sup>. At  
35 lithostatic pressures, this is achieved at depths of ~90–100 km below the Earth’s surface<sup>4</sup>.

36 Geodynamic calculations show that mafic oceanic crust transported into the mantle at  
37 convergent plate margins cannot be exhumed by buoyancy alone after reaching ~50–60 km ( $P$  =  
38 1.4–1.8 GPa)<sup>5</sup>, although felsic continental crust remains positively buoyant to much greater  
39 depths (85–160 km;  $P$  = 2.6–5 GPa)<sup>6</sup>. These results corroborate observations from the rock  
40 record that most UHP mafic eclogite occurs in orogenic (Type B) geological settings<sup>3,7</sup>, where  
41 dismembered meta-mafic pods are encased within high-temperature/low-pressure felsic  
42 orthogneiss<sup>8</sup>. These mafic components represent dikes or sills intruded into the shallow levels of  
43 continental crust prior to collisional orogeny, with the leading edge of the continental margin  
44 thinned, subducted, metamorphosed, and exhumed after detachment from the preceding oceanic  
45 lithosphere<sup>9</sup>. By contrast, eclogite types A, C, and D represent fragments of exhumed oceanic  
46 crust<sup>5</sup> are not genetically associated with continental crustal materials.

47           The oldest UHP continental (Type-B) eclogite on Earth (630 Ma) occurs in the Pan  
48 African orogenic belt, Southwestern Brazil<sup>7</sup>, although oceanic-type UHP eclogite has recently  
49 been reported from the c. 1.8 Ga Nagssugtoqidian Orogen of West Greenland<sup>10</sup>. Additionally, the  
50 oldest continental (Type-B) HP eclogite (c. 2.09 Ga) is located in Cameroon and formed during  
51 the Eburnian collisional orogeny<sup>11</sup>. These occurrences support the low density of felsic  
52 continental crust being a critical factor that allows exhumation of these subducted terranes back  
53 to the Earth's surface<sup>12</sup>. Given multiple independent lines of evidence for subduction and  
54 collisional orogenesis having operated on Earth since at least the middle Archean (c. 3 Ga)<sup>14</sup>, the  
55 absence of (U)HP eclogite in the rock record older than c. 2 Ga is unexpected.

56           In this study, we test the petrophysical implications of recent geochemical proxy analysis  
57 showing that juvenile continental crust on the early Earth was significantly more mafic than  
58 previously thought<sup>15,16</sup>. Thermodynamic phase equilibrium modelling of reconstructed bulk  
59 compositions for Archean, Proterozoic, and Phanerozoic upper continental crust (UCC) and  
60 continental basalt shows that the 'point of no return' for slivers of Archean continents  
61 transported to mantle depths is reached before the HP–UHP transition. By contrast, more silica-  
62 rich Phanerozoic and Proterozoic UCC remains positively buoyant to much greater depths, and  
63 so may be readily exhumed. This secular change in density contrast is independent of hydration  
64 state and implies that UHP rocks likely formed on the early Earth by transport of crustal  
65 materials to mantle depths, yet could not be returned to the surface via buoyancy alone.

66

## 67 **MODELS OF SECULAR CHANGE IN CONTINENTAL CRUST COMPOSITION**

68 Early studies of continental crust composition using surface sampling, weighted compositions of  
69 stratigraphic successions, and/or crustal xenoliths produced conflicting interpretations due to the

70 different levels of exposure and tectonic histories of each studied region<sup>17,18</sup>. In response, ref. 19  
71 combined geochemical analyses with isotopic data to consider only juvenile lithological  
72 components and interpreted that the UCC has remained dacitic in bulk composition ( $\text{SiO}_2 = 65\text{--}$   
73  $67$  wt. %) since c. 3.5 Ga (Fig. 1). However, recently, various geochemical proxies infer that the  
74 maficity ( $\text{FeO} + \text{MgO}$ ) of UCC has shown greater change through time. Ref. 20 used changing  
75 Ti isotope and Ni/Co ratios of terrigenous sediments to suggest that Archean UCC had a  
76 relatively lower (andesitic) bulk  $\text{SiO}_2$  content of  $\sim 62$  wt. % (Fig. 1). By contrast, ref. 15 used  
77 Cu/Ag ratios in glacial diamictites to show that the UCC contained significant volumes of mafic  
78 and ultramafic components at c. 3.0 Ga, and transitioned to a felsic-rock-dominated crust at c.  
79 2.4 Ga, with minimal change since (Fig. 1). These latter findings match calculated Rb/Sr ratios  
80 of juvenile volcanic and plutonic igneous rocks showing that the pre-3 Ga bulk continental crust  
81 was mafic in composition ( $\sim 50$  wt. %  $\text{SiO}_2$ ), and evolved to felsic values ( $\sim 58$  wt. %  $\text{SiO}_2$ )  
82 during the Proterozoic<sup>21</sup>. This change is also consistent with c. 3.7–3.8 Ga immature clastic  
83 metasediments from the Eoarchean Isua complex, west Greenland, that have mafic  
84 compositions<sup>22</sup>, implying a  $\text{SiO}_2$ -poor UCC (Fig. 2).

85         Here, we undertook modelling to quantify the petrophysical implications of these  
86 interpretations that Archean UCC was more mafic than previously thought, which involved  
87 determining mineral assemblages and bulk densities for UCC lithologies in Type-B orogenic  
88 terranes that may be transported to mantle depths via subduction. As fluid content can control  
89 reaction progress during metamorphism, we considered both nominally anhydrous (NAn) and  
90 minimally hydrated (MHy) conditions, which represent endmembers of a spectrum of fluid  
91 contents documented in nature<sup>23</sup>. Calculations were also performed for anhydrous mantle  
92 pyrolite, and the density contrast between each lithology at any given  $P$ – $T$  condition was used to

93 determine whether buoyancy-driven exhumation was possible<sup>24</sup>, assuming the crustal  
94 components could mechanically detach from the descending lithosphere<sup>25</sup>.

95       Secular variation was initially modelled using the reconstructed lithological proportions  
96 for Archean (3 Ga), Paleoproterozoic (2.4 Ga), and Phanerozoic (0.3 Ga) UCC from ref. 15.  
97 Average compositions for greenstone/continental basalt of the same ages<sup>26</sup> were considered as  
98 mafic intrusions into these continental terranes, thus representing a precursor condition for  
99 generating Type B orogenic eclogites. We chose the Archean UCC composition from ref. 15  
100 defined by komatiite–basalt–felsic rock proportions of 20:69:11, which produces a SiO<sub>2</sub> content  
101 of ~51 wt. % matching independently calculated compositions of juvenile continental crust at  
102 that time (~50 wt. %) <sup>21</sup>. We subsequently applied a Monte Carlo analysis<sup>27</sup> to determine the  
103 sensitivity of our results with respect to uncertainty in lithological components reported by ref.  
104 15 for UCC through time (see Supplementary Information; Figs. S4–S5).

105       Representative profiles through each continental crust are given in Fig. 2, with the UCC  
106 representing the top third of each column<sup>27</sup>. While the composition of UCC is not always  
107 equivalent to the entire continental crust, we focused on this uppermost domain for two reasons.  
108 First, analogue<sup>29</sup> and numerical<sup>30</sup> modelling shows that it is UCC that is thinned and stretched at  
109 the leading edge of a terrane margin during continental subduction, and so is carried to eclogite-  
110 facies conditions. Second, in the case of wholesale continental subduction, it is the uppermost  
111 surface of the slab that will be preferentially weakened and detached due to deformation and  
112 fluid–rock interactions at the plate interface<sup>31</sup>. All calculations were performed using the Gibbs  
113 free energy minimization program Theriak-Domino<sup>32</sup> and thermodynamic dataset ds-62 (ref. 33).  
114 All modelling parameters are outlined in the Methods section.

115

## 116 RESULTS

117 Plots of density versus  $P$ - $T$  conditions for each crustal lithology, age, and hydration state are  
118 shown in Fig. 3. Modebox plots showing evolving phase proportions during metamorphism are  
119 given in Figs. S1–S3. If subducted UCC is minimally hydrated with aqueous fluid – as suggested  
120 by field investigation<sup>23</sup> – basaltic intrusions of all ages transform to mafic eclogite (Fig. S1) and  
121 become denser than pyrolite at 2.2–2.3 GPa and 600–640 °C (Fig. 3A). Mafic Archean UCC  
122 follows a similar evolution during descent, becoming denser than surrounding mantle at ~2.4  
123 GPa (Fig. 3A); equivalent to ~75 km depth within the Earth and before the HP–UHP transition is  
124 crossed. Minimally hydrated granodioritic Phanerozoic and Proterozoic UCC contains jadeitic  
125 clinopyroxene, garnet, muscovite (phengite), and quartz/coesite at HP/UHP conditions, with or  
126 without rutile and glaucophane (Fig. S1). Calculated bulk-rock densities of 2.9–3.2 g/cm<sup>3</sup> always  
127 show positive buoyancy compared to the upper mantle (3.35 g/cm<sup>3</sup>; Fig. 3A). A composite  
128 orogenic Type-B terrane with a UCC:basalt volume ratio of 90:10 would reach a point-of-no-  
129 return of  $P \sim 2.3$  GPa during the Archean (Fig. 3B), whereas more silica-rich Proterozoic and  
130 Phanerozoic crust remains positively buoyant up to at least ~3.5 GPa.

131 Calculated  $P$ - $T$ -density profiles for nominally anhydrous lithologies metamorphosed  
132 along this geotherm (Fig. 3C) are different to results obtained assuming fluid saturation. All  
133 mafic crustal components – including bulk Archean UCC – transform to eclogite (Fig. S2) and  
134 show densities of 3.45–3.55 g/cm<sup>3</sup> (Fig. 3C), making them negatively buoyant compared to  
135 pyrolite. Intermediate Proterozoic and Phanerozoic UCC transforms to garnet-, kyanite-, and  
136 jadeite-bearing quartzofeldspathic gneiss during subduction (Fig. S2), which have a bulk density  
137 of 2.8–3.0 g/cm<sup>3</sup> at  $P < 1.2$  GPa and 3.0–3.1 g/cm<sup>3</sup> at the HP–UHP transition (Fig. 3C). These  
138 younger UCC components thus never achieve negative buoyancy within the limits of this model

139 ( $P \sim 3.5$  GPa) and may be readily exhumed if they can separate from the remainder of the  
140 sinking slab. A plot of bulk-terrane density for nominally anhydrous crustal components (Fig.  
141 3D) shows that an Archean UCC that is mafic in composition always remains negatively buoyant  
142 compared to pyrolite. By contrast, both Proterozoic and Phanerozoic terranes have lower  
143 densities ( $\sim 2.9\text{--}3.2$  g/cm<sup>3</sup>) than surrounding mantle, akin to model results for minimal fluid  
144 saturation (Fig. 3B). The results of Monte Carlo sensitivity analysis support these data, with  
145  $\sim 90\%$  of randomised Archean UCC compositions showing the same shift from positive to  
146 negative buoyancy during descent before the HP–UHP transition is reached (Fig. S5).

147

## 148 **DISCUSSION**

149 The age of onset of plate tectonics on Earth is strongly debated<sup>14</sup>, but relies fundamentally on  
150 identifying evidence for subduction having operated at different points in time. Many reliable  
151 indicators of subduction are petrological, such as blueschists, which only form along cold  
152 geothermal gradients<sup>34</sup>; however, no blueschists occur in the geological record before c. 0.8 Ga<sup>35</sup>.  
153 UHP metamorphism is also diagnostic of transporting crustal materials into the mantle<sup>8</sup>. The  
154 oldest UHP eclogite on Earth formed at a similar time (c. 0.6 Ga) to the oldest blueschists, which  
155 has spurred arguments for a very recent onset of plate tectonics<sup>36</sup>. Nonetheless, older HP eclogite  
156 in orogenic terranes occurs as far back in the rock record as c. 2.09 Ga<sup>10</sup> and provides clear  
157 evidence for convergent margin processes during the Proterozoic.

158 Calculated densities for different continental terranes in this work (Fig. 3B, D) show that  
159 the reported high maficity of Archean UCC would have prohibited buoyancy-driven exhumation  
160 once UHP conditions were reached. While we consider subduction as the transport mechanism,  
161 as many lines of evidence support its operation during the Archean<sup>37</sup>, our results notably hold

162 true even if transport into the mantle occurred via dripping or delamination of lower crust in a  
163 stagnant lid geodynamic regime<sup>38</sup>. Metamorphic phase changes in low- and high-MgO Archean  
164 metabasalt experiencing ‘sagduction’-type vertical transport into the mantle shows that eclogite-  
165 facies assemblages acquire negative buoyancy before the HP–UHP transition is reached<sup>39</sup>. The  
166 paucity of felsic material at lower crustal levels<sup>27</sup> (Fig. 2) further reduces the likelihood of these  
167 drips returning to the surface, unless driven by external forces. For subduction of a thinned  
168 continental margin immediately before collisional orogenesis, akin to formation of UHP  
169 eclogites in the Himalayan Range<sup>9</sup>, we also note that our modelling focuses on the density of the  
170 UCC only, not the entire subducted slab. Nonetheless, field-based investigations and numerical  
171 modelling studies show that formation of UHP orogenic eclogite must involve whole-scale  
172 detachment of the continental terrane from the subducting mantle lithosphere due to localized  
173 strain weakening/grain size reduction, hydration, or melting<sup>5,25</sup>. If the proto-exhumed terrane  
174 cannot mechanically detach from the downgoing root, the relative density contrast between UCC  
175 and pyrolite (Fig. 3) becomes irrelevant, as total slab density will always exceed that of  
176 surrounding mantle. This confirms the importance of secular compositional variation when  
177 interpreting changes in geodynamic processes through time<sup>40</sup>, as the absence of (U)HP eclogite  
178 in Archean terranes is often alternatively attributed to overprinting following exhumation.

179         The Archean continental crust being more mafic than previously assumed has several  
180 broader implications for early Earth tectonics and continental hypsometry. Geodynamic models  
181 of the early Earth often assume continental crust to be broadly felsic and employ wet quartzite  
182 flow laws<sup>41</sup>; however, if volumetrically dominated by basalt<sup>15</sup>, a diabase flow law would be more  
183 appropriate. Further, when considering secular changes in both maficity and mantle potential  
184 temperature<sup>42</sup>, the material strength of the Archean continents is markedly different to

185 Phanerozoic equivalents. Calculated yield strength envelopes<sup>43</sup> reveal (Fig. 4A) that Archean  
186 continental crust is contiguous in strength, exhibiting a “crème brulee” type of behaviour, as  
187 opposed to the Phanerozoic “jelly sandwich” model with a weak lower crust<sup>44</sup>. Indeed, its  
188 mechanical properties more closely resemble those of modern oceanic crust than modern  
189 continents, with this relationship holding true for both nominally anhydrous and minimally fluid  
190 saturated end-member scenarios (Fig. 4A).

191 Models for vertical transport of lower crustal continental material into the mantle are  
192 characterised by two end members<sup>45</sup>: short-wavelength drips (e.g. Rayleigh-Taylor instabilities)  
193 or longer-wavelength ‘peels’ (e.g. delamination). A prerequisite for delamination is the presence  
194 of a weak layer at the point of separation<sup>45</sup>, thus allowing the lower continental crust to  
195 rheologically separate into contiguous layers. However, as the calculated yield strength envelope  
196 (Fig. 4A) for a mafic Archean continental crust does not exhibit a pronounced weak layer, unlike  
197 Phanerozoic continental crust, this implies that the primary mechanism for recycling of  
198 continental material into the mantle was dripping, in agreement with geodynamical models<sup>46</sup>.  
199 Finally, the above-average density ( $\sim 2.87 \text{ g cm}^{-3}$ ) and reduced thickness of Archean continents  
200 compared to Phanerozoic continents (Fig. 2) lowers the average isostatic elevation of the former  
201 by around 2.2 km relative to that of the present day (Fig. 4B)<sup>47</sup>. This implies that the early Earth  
202 was likely covered by a global ocean with an average depth over the continental surface of  $-1.3$   
203 km, in agreement with recent isotopic data<sup>48</sup>. The transition to more felsic continental crust at the  
204 end of the Archean (Figs 1–2) and the resulting change in isostatic balance supports models of  
205 changing freeboard over time that imply a Late Archean (c. 2.5 Ga) emergence of the  
206 continents<sup>49</sup>. This, in turn, facilitated the onset of the Great Oxygenation Event soon  
207 afterwards<sup>50</sup>, paving the way for the development of complex life on Earth.

208 **METHODS**

209 **Petrological modelling**

210 Petrological modelling used to investigate the metamorphic phase transformations and density  
211 variations in all rock types was performed using Theriak-Domino<sup>32</sup> and the internally consistent  
212 thermodynamic dataset ds-62 (ref. 33). Phase equilibria for pyrolite<sup>51</sup> were calculated in the  
213 Na<sub>2</sub>O–CaO–FeO–MgO–Al<sub>2</sub>O<sub>3</sub>–SiO<sub>2</sub>–O<sub>2</sub>–Cr<sub>2</sub>O<sub>3</sub> (NCFMASOCr) system using activity–  
214 composition (*a*–*X*) relations for olivine, garnet, clinopyroxene, orthopyroxene, spinel,  
215 plagioclase, and ultramafic silicate melt<sup>52</sup>. Phase equilibria for all crustal materials were  
216 calculated in the Na<sub>2</sub>O–CaO–K<sub>2</sub>O–FeO–MgO–Al<sub>2</sub>O<sub>3</sub>–SiO<sub>2</sub>–H<sub>2</sub>O–TiO<sub>2</sub>–O<sub>2</sub> (NCKFMASHTO)  
217 system using *a*–*X* relations for: clinopyroxene (diopside–omphacite–jadeite) and clinoamphibole  
218 (glaucophane–actinolite–hornblende)<sup>53</sup>; garnet, biotite, chloritoid, muscovite–paragonite, and  
219 chlorite<sup>54</sup>; epidote<sup>33</sup>; plagioclase<sup>55</sup>; and ilmenite<sup>56</sup>. Pure phases included aqueous fluid (H<sub>2</sub>O) talc,  
220 lawsonite, kyanite, quartz, rutile, titanite, and albite.

221 Two end-member hydration states were used for each crustal lithology: nominally  
222 anhydrous (NAn) and minimally hydrated (MHy). The former considered 1 mol. % H<sub>2</sub>O within  
223 the bulk-rock composition, after ref. 15, and the latter considered a lithology-specific fluid  
224 content that allowed minimal free H<sub>2</sub>O within the equilibrium phase assemblage during  
225 subduction. For mafic lithologies, this was ~10–13 mol. % (Table S2), which is comparable to  
226 measured H<sub>2</sub>O contents in modern-day hydrated oceanic crust<sup>57</sup>. A bulk-rock Fe<sup>3+</sup>/Fe<sup>total</sup> ratio of  
227 0.1 was applied to all rock types based on refs. 58 and 59; however, variation within the bounds  
228 of accepted uncertainty is unlikely to have any significant effect on calculated phase equilibria  
229 and/or petrophysical properties. Calculations were performed using pressure–temperature (*P*–*T*)  
230 conditions defined for the slab surface of subducted crust in an ‘average’ subduction zone<sup>60</sup>,

231 which was defined from a compilation of exhumed (U)HP blueschist- and eclogite-facies rocks  
232 in Phanerozoic and Proterozoic terranes. This geotherm, however, is comparable to that  
233 purported for the late Archean based on geochemical modeling of tonalite–trondhjemite–  
234 granodiorite magma petrogenesis<sup>61</sup>, so is considered here for subducted crusts of all ages to  
235 allow direct comparison of density profiles.

236 Sensitivity analysis of the uncertainty on UCC density and metamorphosed petrological  
237 constitution based on uncertainty in pre-subduction lithological proportions for Archean terranes  
238 was performed as outlined in the Supplementary Information. This analysis demonstrates that the  
239 ‘depth of no return’ for most plausible iterations of subducted Archean UCC occurs consistently  
240 (~90% of all randomized bulk compositions) before the HP–UHP transition is reached.

241

## 242 **Lithospheric strength modelling**

243 We calculate yield strength envelopes<sup>43</sup> where failure is assumed to occur either by brittle  
244 deformation, governed by Byerlee’s friction coefficients<sup>62</sup>, or ductile flow<sup>63</sup> of the form

$$245 \quad \dot{\epsilon} = A\tau^n \exp\left(-\frac{E + PV}{RT}\right), \quad (1)$$

246 where  $\dot{\epsilon}$  represents strain rate (taken to be  $10^{-14} \text{ s}^{-1}$ ),  $\tau$  deviatoric stress,  $P$  and  $T$  are pressure and  
247 temperature, respectively,  $R$  is the gas constant, and  $(A, E, V, n)$  are material parameters. We use  
248 a thermal model<sup>39</sup> for Archean and Phanerozoic lithosphere with mantle potential temperatures  
249 of  $1650 \text{ }^\circ\text{C}$  and  $1330 \text{ }^\circ\text{C}$ , respectively<sup>42</sup>, and material parameters for olivine<sup>64</sup>, diabase<sup>65</sup>, and  
250 quartzite<sup>66</sup> for the structures illustrated in Fig. 4A. Material parameters for dry and wet flow laws  
251 are utilised for the nominally anhydrous and minimally hydrated end-member cases.

252

## 253 **Isostatic balance calculation**

254 At the length scales of the continents, flexural effects may safely be neglected<sup>67</sup> and we model  
 255 isostasy using a vertical balance, incorporating aspects of Airy<sup>68</sup> and Pratt<sup>69</sup> isostasy. The  
 256 pressure at the depth of compensation,  $D_c$ , (Fig. 4B) beneath oceanic lithosphere is given by

$$257 \quad P_o = [(\rho_w - \rho_m)h_o + (\rho_o - \rho_m)T_o + D_c\rho_m] g, \quad (2)$$

258 and that for continental lithosphere in the Phanerozoic

$$259 \quad P_c = [\rho_c h_c + (\rho_c - \rho_m)(T_c - h_c) + D_c\rho_m] g, \quad (3)$$

260 where  $\rho$  = density; w = water; o = oceanic lithosphere; m = asthenospheric mantle; c =  
 261 phanerozoic continental crust;  $h_o$  = water depth,  $h_c$  = topographic expression of the continents;  $T_o$   
 262 and  $T_c$  = thickness of the oceanic and continental crust respectively; and  $g$  = acceleration due to  
 263 gravity. As the pressure will be equal at the depth of compensation, we can equate these two  
 264 expressions and rearrange to solve for the average topographic expression of the continents,  $h_c$ ,

$$265 \quad h_c = \frac{\rho_m - \rho_c}{\rho_m} T_c - \frac{\rho_m - \rho_w}{\rho_m} h_o - \frac{\rho_m - \rho_o}{\rho_m} T_o \quad (4)$$

266 For typical values (Table S3) of Phanerozoic crust we retrieve values close to that of average  
 267 modern continental topography (900 m) and adjusting the crustal thickness by 800 m produces  
 268 an exact match. We then apply this model to Archean crustal values (Table S3), and replace the  
 269 continental density  $\rho_c$  with

$$270 \quad \rho_{cA} = (1 - \lambda)\rho_c + \lambda\rho_o, \quad (5)$$

271 with  $\rho_{cA}$  = density of Archean crust, and  $\lambda$  represents the basalt volume fraction in Archean  
 272 continental crust. However, we retrieve a negative value (-1.2 km) for the average topography,  
 273 indicating the continents were submerged. This violates our assumption that the continents were  
 274 above the ocean surface and requires two modifications to the model: firstly, the water would  
 275 represent an additional load in the isostatic balance calculation, and secondly, redistributing the

276 volume of water across the whole planet would reduce the average water depth ( $h_o$ ) over oceanic  
277 crust. Accounting for the redistribution of water and reversing the polarity of  $h_c$  as it now  
278 represents water depth above the continents gives

$$279 \quad h_{oA} = h_o - \frac{3}{7}h_{cA}, \quad (6)$$

280 with  $h_{oA}$  the water depth over Archean oceanic crust and  $h_{cA}$  the water depth over Archean  
281 continental crust. Here, we have assumed here that the volume of water present on the Earth  
282 during the Archean was no less than it is in the present day, as any additional volume would  
283 serve only to increase the water depth uniformly everywhere. Hence, equation (4) can be  
284 reframed as:

$$285 \quad h_{cA} = \frac{7}{10} \left( h_o + \frac{\rho_m - \rho_o}{\rho_m - \rho_w} T_o - \frac{\rho_m - \rho_{cA}}{\rho_m - \rho_w} T_c \right), \quad (7)$$

286 and  $h_{cA}$  is interpreted as a lower bound on Archean water depth. When applied to Archean  
287 parameters (Table S3) we retrieve an average water depth over the continents of 1.3 km and a  
288 reduction in water depth over the oceans of 600 m relative to present day values.

289

## 290 **DATA AVAILABILITY**

291 All data required to reproduce the results of our modelling is provided in the Methods section  
292 and Supplementary Information.

293

## 294 **CODE AVAILABILITY**

295 Codes for reproducing the isostatic balance calculation and yield strength envelopes may be  
296 found at [www.jamesdpmoore.com](http://www.jamesdpmoore.com).

297

298 **REFERENCES**

- 299 1. Häüy, R., 1822. *Traité de Minéralogie*, 2nd edn. Bachelier et Huzar, Paris.
- 300 2. Coleman, R.G., Lee, D.E., Beatty, L.B., & Brannock, W.W. Eclogites and eclogites: their  
301 differences and similarities. *Geol. Soc. Am. Bull.* **76**, 483–508 (1965).
- 302 3. Hacker, B.R. Pressures and temperatures of ultrahigh-pressure metamorphism:  
303 implications for UHP tectonics and H<sub>2</sub>O in subducting slabs. *Int. Geol. Rev.* **48**, 1053–1066  
304 (2006).
- 305 4. Hernández-Uribe, D., & Palin, R.M., 2019. A revised petrological model for subducted  
306 oceanic crust: Insights from phase equilibrium modelling. *J. Metamorph. Geol.*, **37**, 745–  
307 768.
- 308 5. Agard, P., Yamato, P., Jolivet, L., & Burov, E. Exhumation of oceanic blueschists and  
309 eclogites in subduction zones: timing and mechanisms. *Earth-Sci. Rev.* **92**, 53–79 (2009).
- 310 6. Chapman, T., Clarke, G.L., & Daczko, N.R. The role of buoyancy in the fate of ultrahigh  
311 pressure eclogite. *Sci. Rep.* **9**, 1–9 (2019).
- 312 7. Liou, J.G., Ernst, W.G., Zhang, R.Y., Tsujimori, T., & Jahn, B.M. Ultrahigh-pressure  
313 minerals and metamorphic terranes – The view from China. *J. Asian Earth Sci.* **35**, 199–  
314 231 (2009).
- 315 8. Gilotti, J.A. The realm of ultrahigh-pressure metamorphism. *Elements*, **9**, 255–260 (2013).
- 316 9. St-Onge, M.R., Rayner, N., Palin, R.M., Searle, M.P., & Waters, D.J. Integrated pressure–  
317 temperature–time constraints for the Tso Morari dome (Northwest India): implications for  
318 the burial and exhumation path of UHP units in the western Himalaya. *J. Metamorph.*  
319 *Geol.* **31**, 469–504 (2013).
- 320 10. Glassley, W.E., Korstgård, J.A., Sørensen, K., & Platou, S.W. A new UHP metamorphic

- 321 complex in the ~1.8 Ga Nagssugtoqidian Orogen of West Greenland. *Am. Mineral.*, **99**,  
322 1315–1334 (2014).
- 323 11. Loose, D., & Schenk, V. 2.09 Ga old eclogites in the Eburnian-Transamazonian orogen of  
324 southern Cameroon: Significance for Palaeoproterozoic plate tectonics. *Precambrian Res.*  
325 **304**, 1–11 (2018).
- 326 12. Boutelier, D., Chemenda, A., & Jorand, C. Continental subduction and exhumation of  
327 high-pressure rocks: insights from thermo-mechanical laboratory modelling. *Earth Planet.*  
328 *Sci. Lett.* **222**, 209–216 (2004).
- 329 13. Hawkesworth, C.J., Cawood, P.A., & Dhuime, B. Tectonics and crustal evolution. *GSA*  
330 *Today*, 9, 4–11 (2016).
- 331 14. Palin, R.M., Santosh, M., Cao, W., Li, S.S., Hernández-Uribe, D., & Parsons, A. Secular  
332 change and the onset of plate tectonics on Earth. *Earth-Sci. Rev.*, **207**, 103172 (2020).
- 333 15. Chen, K. *et al.* How mafic was the Archean upper continental crust? Insights from Cu and  
334 Ag in ancient glacial diamictites. *Geochim. Cosmochim. Acta* **278**, 16–29 (2020).
- 335 16. Tang, M., Chen, K., & Rudnick, R.L. Archean upper crust transition from mafic to felsic  
336 marks the onset of plate tectonics. *Science*, **351**, 372–375 (2016).
- 337 17. Holland, J.G., & Lambert, R.S.T. Major element chemical composition of shields and the  
338 continental crust. *Geochim. Cosmochim. Acta* **36**, 673–683 (1972).
- 339 18. Taylor, S.R., & McLennan, S.M. The geochemical evolution of the continental crust. *Rev.*  
340 *Geophys.*, **33**, 241–265 (1995).
- 341 19. Condie, K.C. Chemical composition and evolution of the upper continental crust:  
342 contrasting results from surface samples and shales. *Chem. Geol.* **104**, 1–37 (1993).
- 343 20. Greber, N.D. *et al.* Titanium isotopic evidence for felsic crust and plate tectonics 3.5

- 344 billion years ago. *Science*, **357**, 1271–1274 (2017).
- 345 21. Dhuime, B., Wuestefeld, A., & Hawkesworth, C.J. Emergence of modern continental crust  
346 about 3 billion years ago. *Nature Geosci.* **8**, 552–556 (2015).
- 347 22. Bolhar, R., Kamber, B.S., Moorbath, S., Whitehouse, M., & Collerson, K.D. Chemical  
348 characterization of Earth’s most ancient clastic metasediments from the Isua Greenstone  
349 belt, southern west Greenland. *Geochim. Cosmochim. Acta* **69**, 1555–1573 (2005).
- 350 23. Deming, D. Fluid flow and heat transport in the upper continental crust. *Geol. Soc. Lond.*  
351 *Spec. Pub.* **78**, 27–42 (1994).
- 352 24. Weller, O.M., Copley, A., Miller, W.G.R., Palin, R.M., & Dyck, B. The relationship  
353 between mantle potential temperature and oceanic lithosphere buoyancy. *Earth Planet. Sci.*  
354 *Lett.* **518**, 86–99 (2019).
- 355 25. Warren, C.J. Exhumation of (ultra)-high-pressure terranes: concepts and mechanisms.  
356 *Solid Earth* **4**, 75–92 (2013).
- 357 26. Condie, K.C., Aster, R.C., & Van Hunen, J. A great thermal divergence in the mantle  
358 beginning 2.5 Ga: Geochemical constraints from greenstone basalts and komatiites.  
359 *Geosci. Front.* **7**, 543–553 (2016).
- 360 27. Rudnick, R.L., & Gao, S. Composition of the continental crust: The crust. **3**, 1–64 (2003).
- 361 28. Palin, R.M., Weller, O.M., Waters, D.J., & Dyck, B. Quantifying geological uncertainty in  
362 metamorphic phase equilibria modelling; a Monte Carlo assessment and implications for  
363 tectonic interpretations. *Geosci. Front.*, **7**, 591–607 (2016).
- 364 29. Bialas, R.W., Funicello, F., & Faccenna, C., 2011. Subduction and exhumation of  
365 continental crust: Insights from laboratory models. *Geophys. J. Int.*, **184**, 43–64 (2011).
- 366 30. Palin, R.M., Reuber, G.S., White, R.W., Kaus, B.J., & Weller, O.M. Subduction

- 367 metamorphism in the Himalayan ultrahigh-pressure Tso Moriri massif: an integrated  
368 geodynamic and petrological modelling approach. *Earth Planet. Sci. Lett.* **467**, 108–119  
369 (2017).
- 370 31. Zheng, Y., Zhao, Z., & Chen, Y. Continental subduction channel processes: Plate interface  
371 interaction during continental collision. *Chinese Sci. Bull.*, **58**, 4371–4377 (2013).
- 372 32. De Capitani, C., & Petrakakis, K. The computation of equilibrium assemblage diagrams  
373 with Theriak/Domino software. *Am. Mineral.* **95**, 1006–1016 (2010).
- 374 33. Holland, T.J.B., & Powell, R. An improved and extended internally consistent  
375 thermodynamic dataset for phases of petrological interest, involving a new equation of  
376 state for solids. *J. Metamorph. Geol.* **29**, 333–383 (2011).
- 377 34. Palin, R.M., & White, R.W. Emergence of blueschists on Earth linked to secular changes  
378 in oceanic crust composition. *Nature Geosci.* **9**, 60–64 (2016).
- 379 35. Maruyama, S., Liou, J.G., & Terabayashi, M. Blueschists and eclogites of the world and  
380 their exhumation. *Int. Geol. Rev.* **38**, 485–594 (1996).
- 381 36. Stern, R.J. Evidence from ophiolites, blueschists, and ultrahigh-pressure metamorphic  
382 terranes that the modern episode of subduction tectonics began in Neoproterozoic time.  
383 *Geology*, **33**, 557–560 (2005).
- 384 37. Shirey, S.B., & Richardson, S.H. Start of the Wilson cycle at 3 Ga shown by diamonds  
385 from subcontinental mantle. *Science*, **333**, 434–436 (2011).
- 386 38. Piccolo, A., Kaus, B.J., White, R.W., Palin, R.M., & Reuber, G.S. Plume–lid interactions  
387 during the Archean and implications for the generation of early continental terranes.  
388 *Gondwana Res.* (2020), doi: 10.1016/j.gr.2020.06.024
- 389 39. Wade, J., Dyck, B., Palin, R.M., Moore, J.D., & Smye, A.J. The divergent fates of

- 390 primitive hydrospheric water on Earth and Mars. *Nature*, **552**, 391–394 (2017).
- 391 40. Weller, O.M., & St-Onge, M.R. Record of modern-style plate tectonics in the  
392 Palaeoproterozoic Trans-Hudson orogen. *Nature Geosci.* **10**, 305–311 (2017).
- 393 41. Sizova, E., Gerya, T., Brown, M. & Perchuk, L.L. Subduction styles in the Precambrian:  
394 Insight from numerical experiments. *Lithos*, **116**, 209–229 (2010).
- 395 42. Herzberg, C., Condie, K., & Korenaga, J. Thermal history of the Earth and its petrological  
396 expression. *Earth Planet. Sci. Lett.* **292**, 79–88 (2010).
- 397 43. Watts, A.B. *Isostasy and Flexure of the Lithosphere*. (2001) Cambridge University Press
- 398 44. Bürgmann, R., & Dresen, G. Rheology of the lower crust and upper mantle: Evidence from  
399 rock mechanics, geodesy, and field observations. *Ann. Rev. Earth Planet. Sci.* **36**, 531–567  
400 (2008).
- 401 45. Beall, A. P., Moresi, L., & Stern T. Dripping or delamination? A range of mechanisms for  
402 removing the lower crust or lithosphere. *Geophys. J. Int.* **210**, 671–692 (2017).
- 403 46. Gerya, T. Precambrian geodynamics: Concepts and models. *Gondwana Res.*, **25**, 442–463  
404 (2014)
- 405 47. Lamb, S., Moore, J.D.P., Perez-Gussinya, M., & Stern, T. Global whole lithosphere  
406 isostasy: implications for surface elevations, strength and densities of the continental  
407 lithosphere. *Geophys. Geochem. Geosys.* (2020), doi: 10.1029/2020GC009150
- 408 48. Johnson, B.W., & Wing, B.A. Limited Archaean continental emergence reflected in an  
409 early Archaean <sup>18</sup>O-enriched ocean. *Nature Geosci.* **13**, 243–248 (2020).
- 410 49. Flament, N., Coltice, N. & Rey, P.F. A case for late-Archaean continental emergence from  
411 thermal evolution models and hypsometry. *Earth Planet. Sci. Lett.* **275**, 326–336 (2008).
- 412 50. Gumsley, A.P. *et al.* Timing and tempo of the Great Oxidation Event. *Proc. Nat. Acad. Sci.*

- 413           **114**, 1811–1816 (2017).
- 414 51. Ringwood, A.E. *Composition and Petrology of the Earth’s Mantle*. MacGraw-Hill, 618  
415           (1975).
- 416 52. Jennings, E.S., & Holland, T.J.B. A simple thermodynamic model for melting of peridotite  
417           in the system NCFMASOCr. *J. Petrol.* **56**, 869–892 (2015).
- 418 53. Green, E.C.R. *et al.* Activity–composition relations for the calculation of partial melting  
419           equilibria in metabasic rocks. *J. Metamorph. Geol.* **34**, 845–869 (2016).
- 420 54. White, R.W., Powell, R., Holland, T.J.B., & Green, E.C.R. New mineral activity–  
421           composition relations for thermodynamic calculations in metapelitic systems. *J.*  
422           *Metamorph. Geol.* **32**, 261–286 (2014).
- 423 55. Holland, T.J.B., & Powell, R. Activity–composition relations for phases in petrological  
424           calculations: an asymmetric multicomponent formulation: *Contrib. Mineral. Petrol.* **145**,  
425           492–501 (2003).
- 426 56. White, R.W., Powell, R., Holland, T.J.B., & Worley, B.A. The effect of TiO<sub>2</sub> and Fe<sub>2</sub>O<sub>3</sub> on  
427           metapelitic assemblages at greenschist and amphibolite facies conditions: mineral  
428           equilibria calculations in the system K<sub>2</sub>O–FeO–MgO–Al<sub>2</sub>O<sub>3</sub>–SiO<sub>2</sub>–H<sub>2</sub>O–TiO<sub>2</sub>–Fe<sub>2</sub>O<sub>3</sub>. *J.*  
429           *Metamorph. Geol.* **18**, 497–511 (2000).
- 430 57. Staudigel, H. Hydrothermal alteration processes in the oceanic crust: *Treat. Geochem.* **3**,  
431           659–681 (2003).
- 432 58. Stagno, V., Ojwang, D.O., McCammon, C.A., & Frost, D.J. The oxidation state of the  
433           mantle and the extraction of carbon from Earth’s interior: *Nature*, **493**, 84–88 (2013).
- 434 59. Le Losq, C. *et al.* Determination of the oxidation state of iron in Mid-Ocean Ridge basalt  
435           glasses by Raman spectroscopy. *Am. Mineral.* **104**, 1032–1042 (2019).

- 436 60. Penniston-Dorland, S.C., Kohn, M.J., & Manning, C.E. The global range of subduction  
437 zone thermal structures from exhumed blueschists and eclogites: Rocks are hotter than  
438 models. *Earth Planet. Sci. Lett.* **428**, 243–254 (2015).
- 439 61. Martin, H., & Moyen, J.F. Secular changes in tonalite-trondhjemite-granodiorite  
440 composition as markers of the progressive cooling of Earth. *Geology*, **30**, 319–322 (2002).
- 441 62. Byerlee, J. Friction of rocks. *Pure Appl. Geophys.*, **116**, 615–626 (1978).
- 442 63. D. L. Kohlstedt, & Hansen, L.N. Constitutive Equations, Rheological Behavior, and  
443 Viscosity of Rocks, vol. 2 (Elsevier B.V., 2015).
- 444 64. Hirth, G., & Kohlstedt, D. Rheology of the upper mantle and the mantle wedge: A view  
445 from the experimentalists. *Geophys. Mono. Am. Geophys. Union* **4**, 1–24 (2003).
- 446 65. S. J. Mackwell, S.J. Zimmerman, M.E., & Kohlstedt, D.L. High-temperature deformation  
447 of dry diabase with application to tectonics on Venus. *J. Geophys. Res.*, **103**, 975–984  
448 (1998).
- 449 66. Hirth, G., Teyssier, C., & Dunlap, J. An evaluation of quartzite flow laws based on  
450 comparisons between experimentally and naturally deformed rocks. *Int. J. Earth Sci.*, **90**,  
451 77–87 (2001).
- 452 67. Watts, A. B., & Moore, J. D. P. Flexural isostasy: Constraints from gravity and topography  
453 power spectra. *J. Geophys. Res.: Solid Earth*, **122**, 8417–8430 (2017).
- 454 68. Airy, G. B. On the computation of the effect of the attraction of mountain masses, as  
455 disturbing the apparent astronomical latitude of stations in geodetic surveys. *Phil. Trans. R.*  
456 *Soc*, **145**, 101–104 (1855).
- 457 69. Pratt, J. H. On the deflection of the plumb-line in India, caused by the attraction of the  
458 Himalaya mountains and of the elevated regions beyond; and its modification by the

459 compensating effect of a deficiency of matter below the mountain mass. *Phil. Trans. R.*  
460 *Soc.* **149**, 745–778 (1859).

461

#### 462 **CORRESPONDING AUTHOR**

463 All correspondence and requests for materials should be addressed to Associate Professor  
464 Richard Palin ([richard.palin@earth.ox.ac.uk](mailto:richard.palin@earth.ox.ac.uk)), Department of Earth Sciences, University of  
465 Oxford, UK.

466

#### 467 **ACKNOWLEDGEMENTS**

468 JDPM acknowledges support from Marsden grant 14-VUW-085, Royal Society of New Zealand.

469

#### 470 **AUTHOR CONTRIBUTIONS**

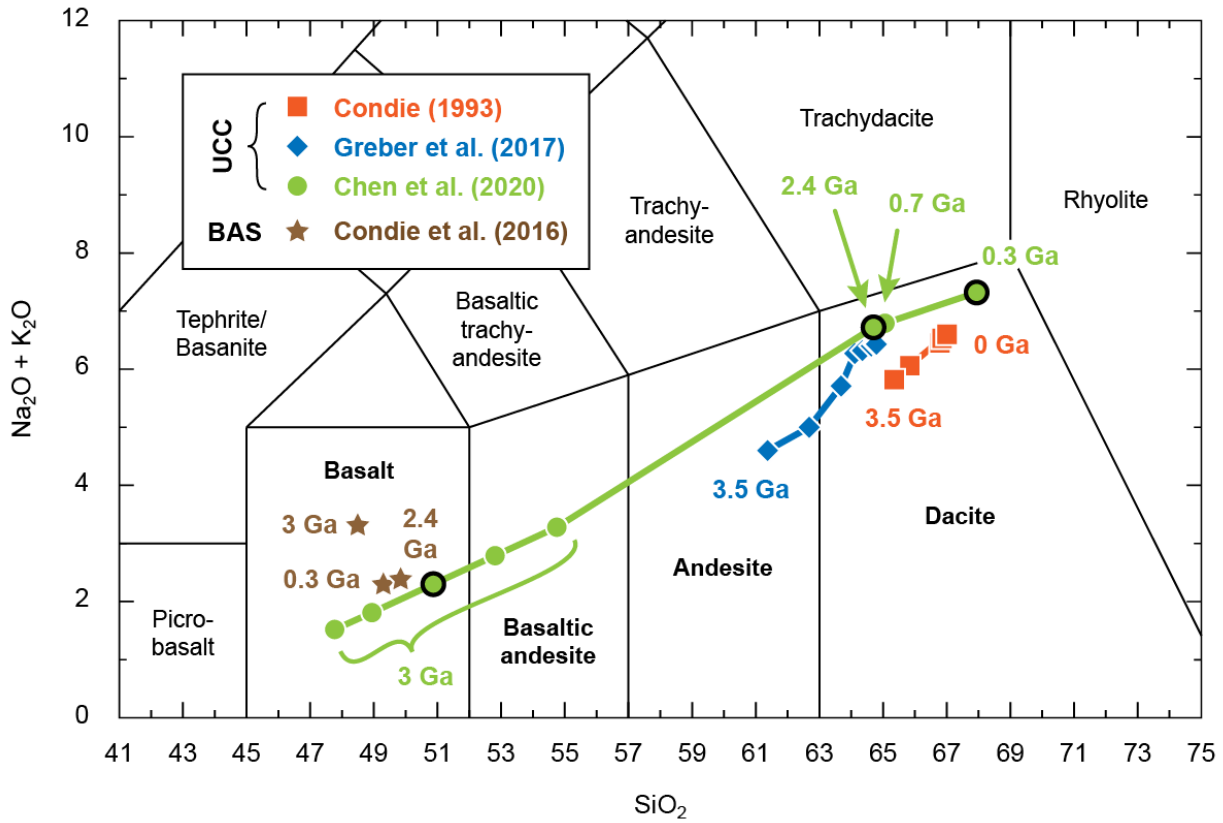
471 RMP devised the study and performed petrological calculations with ZZ and GH. JDPM  
472 calculated yield strength envelopes and isostatic balance models. All authors interpreted the  
473 results and wrote the manuscript.

474

#### 475 **COMPETING INTERESTS**

476 The authors declare no competing interests.

477 **FIGURES**



478

479

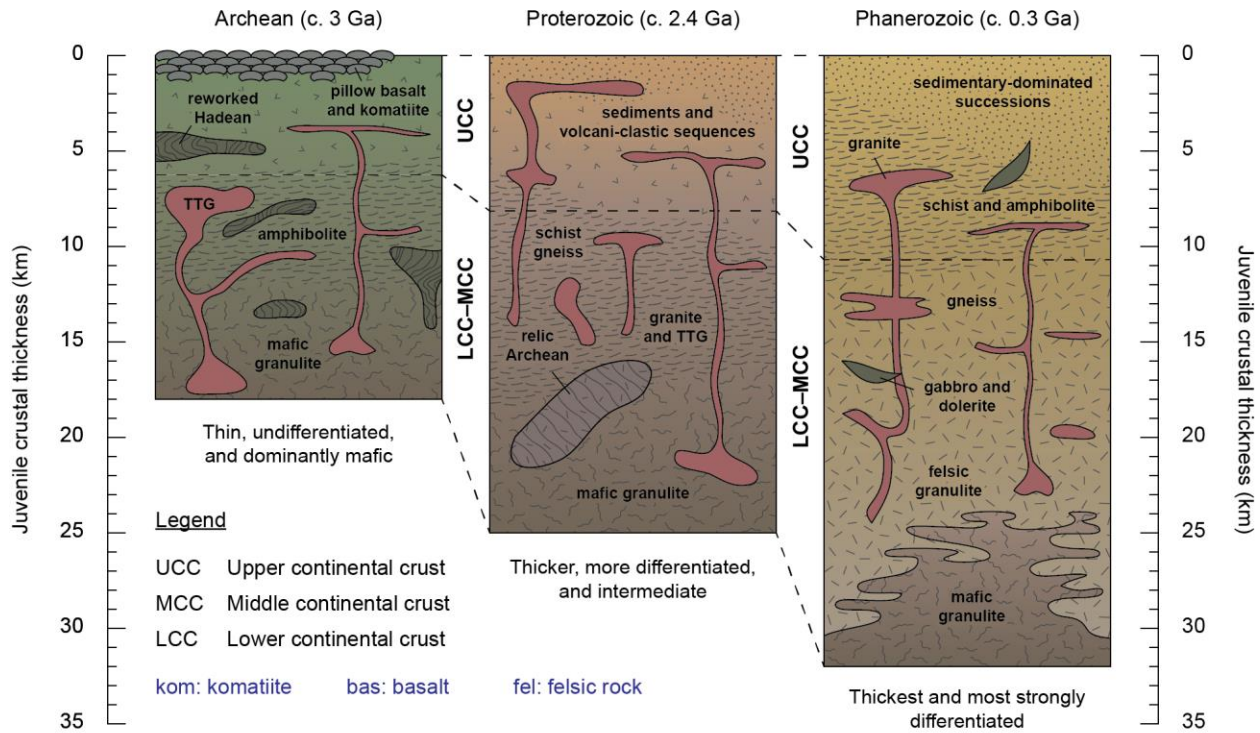
480 **Figure 1. Total alkali–silica diagram showing bulk compositions of crustal lithologies**

481 **considered in this study.** Representative compositions are shown for upper continental crust

482 (UCC) and continental basalt (BAS) of Archean (3 Ga), Proterozoic (2.4 Ga), and Phanerozoic

483 (0.3 Ga) age.

|                                   |             |             |             |
|-----------------------------------|-------------|-------------|-------------|
| UCC lithology (kom:bas:fel)       | 20:69:11    | 0:28:72     | 0:26:74     |
| Bulk UCC SiO <sub>2</sub> content | c. 51 wt. % | c. 65 wt. % | c. 68 wt. % |



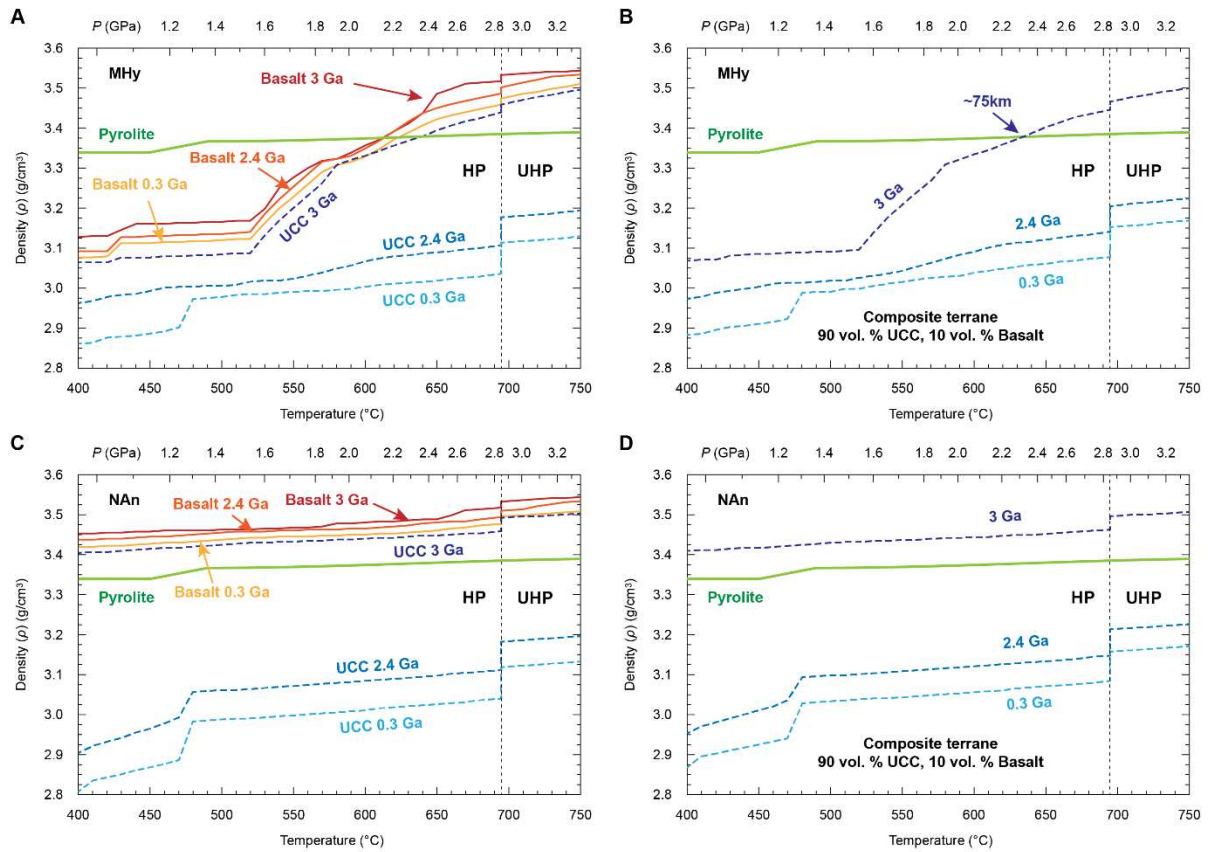
484

485

486 **Figure 2. Secular change in continental crust structure, lithology, and composition through**

487 **time.** Secular changes in reconstructed composition, thickness, and petrological components are

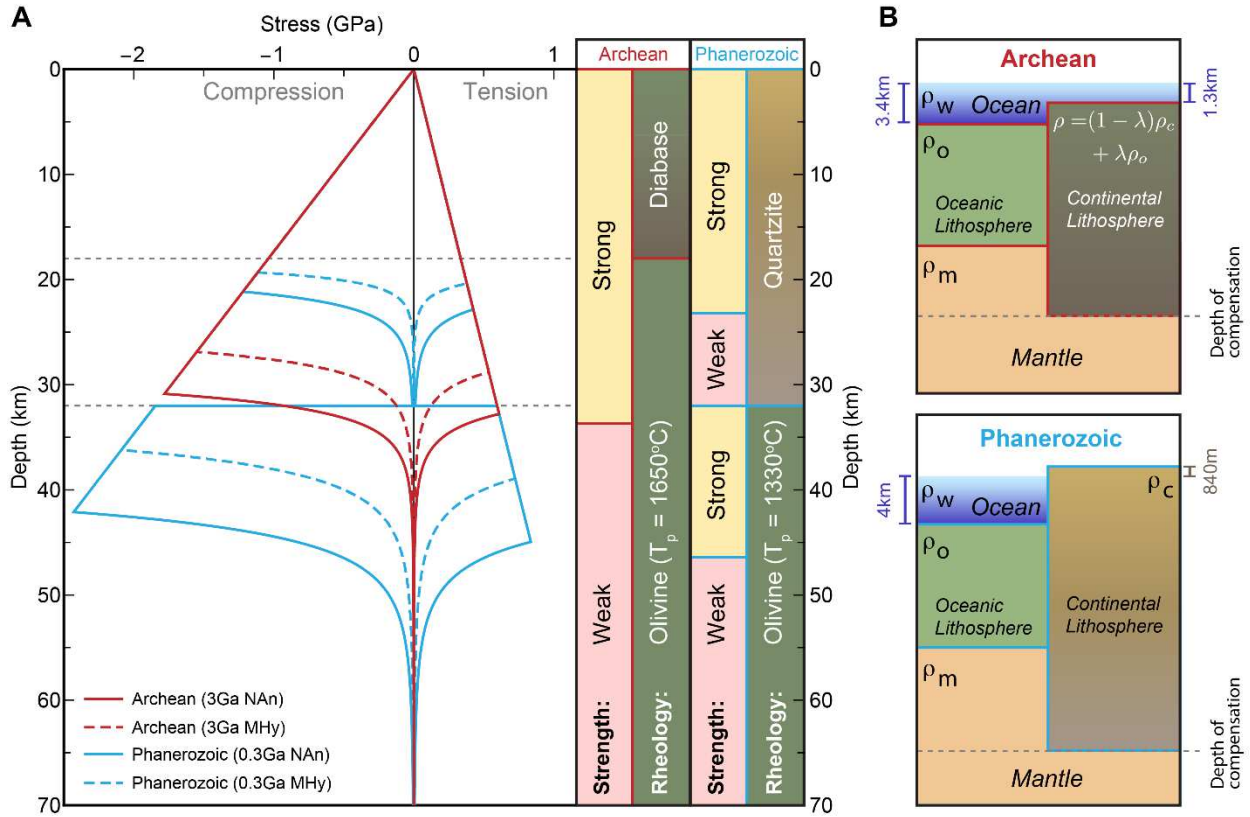
488 emphasised. Phanerozoic and Proterozoic profiles modified with permission after ref. 13.



489

490

491 **Figure 3. Calculated density profiles along a typical subduction zone geotherm.** Values for  
 492 (A) minimally hydrated (MHy) continental crust and basalt and a (B) composite terrane with  
 493 volume proportions of these lithologies in the ratio 90:10, respectively, during metamorphism  
 494 along an average subduction zone pressure–temperature ( $P$ – $T$ ) path. (C–D) As for parts A–B, but  
 495 for nominally anhydrous (NAn) equivalents of each lithology.



496

497

498 **Figure 4. Rheological and hypsometric implications of changes in continental crust**

499 **composition.** (A) Yield strength envelope (YSE) for Archean (red) and Phanerozoic (blue)

500 lithosphere under nominally anhydrous (NAn, solid lines) and minimally hydrated (MHy, dashed

501 lines) conditions. The relative strength of the lithosphere and rheology employed to generate the

502 YSE are shown for reference.  $T_p$  = mantle potential temperature. (B) Schematic cross sections

503 through Archean and Phanerozoic lithosphere demonstrating changes in hypsometry under

504 isostatic equilibrium.  $\rho$  = density; w = water; o = oceanic lithosphere; m = asthenospheric

505 mantle; c = Phanerozoic continental lithosphere;  $\lambda$  = basalt fraction in Archean continental crust.

506 **SUPPLEMENTARY INFORMATION**

507 Supplementary Information is available for this paper:

508 **Figure S1.** Calculated phase equilibria and density profile for all crustal components discussed  
509 herein along the modelled geotherm, assuming a minimally hydrated state.

510 **Figure S2.** Calculated phase equilibria and density profile for all crustal components discussed  
511 herein along the modelled geotherm, assuming a nominally anhydrous state.

512 **Figure S3.** Calculated phase equilibria and density profile for mantle pyrolite along the modelled  
513 geotherm.

514 **Figure S4.** Total alkali–silica (TAS) diagram showing calculated distribution of randomized  
515 Archean (3 Ga) upper continental crust (UCC) bulk compositions used for sensitivity  
516 analysis.

517 **Figure S5.** Results of sensitivity analysis for the density of Archean (3 Ga) upper continental  
518 crust (UCC) during subduction.

519 **Table S1.** Upper continental crust (UCC) compositions (weight % oxide) reconstructed by Chen  
520 et al. (2020).

521 **Table S2.** Bulk-rock compositions used for petrological modelling (mole % oxide).

522 **Table S3.** Parameters used for the isostatic balance calculation.

# Figures

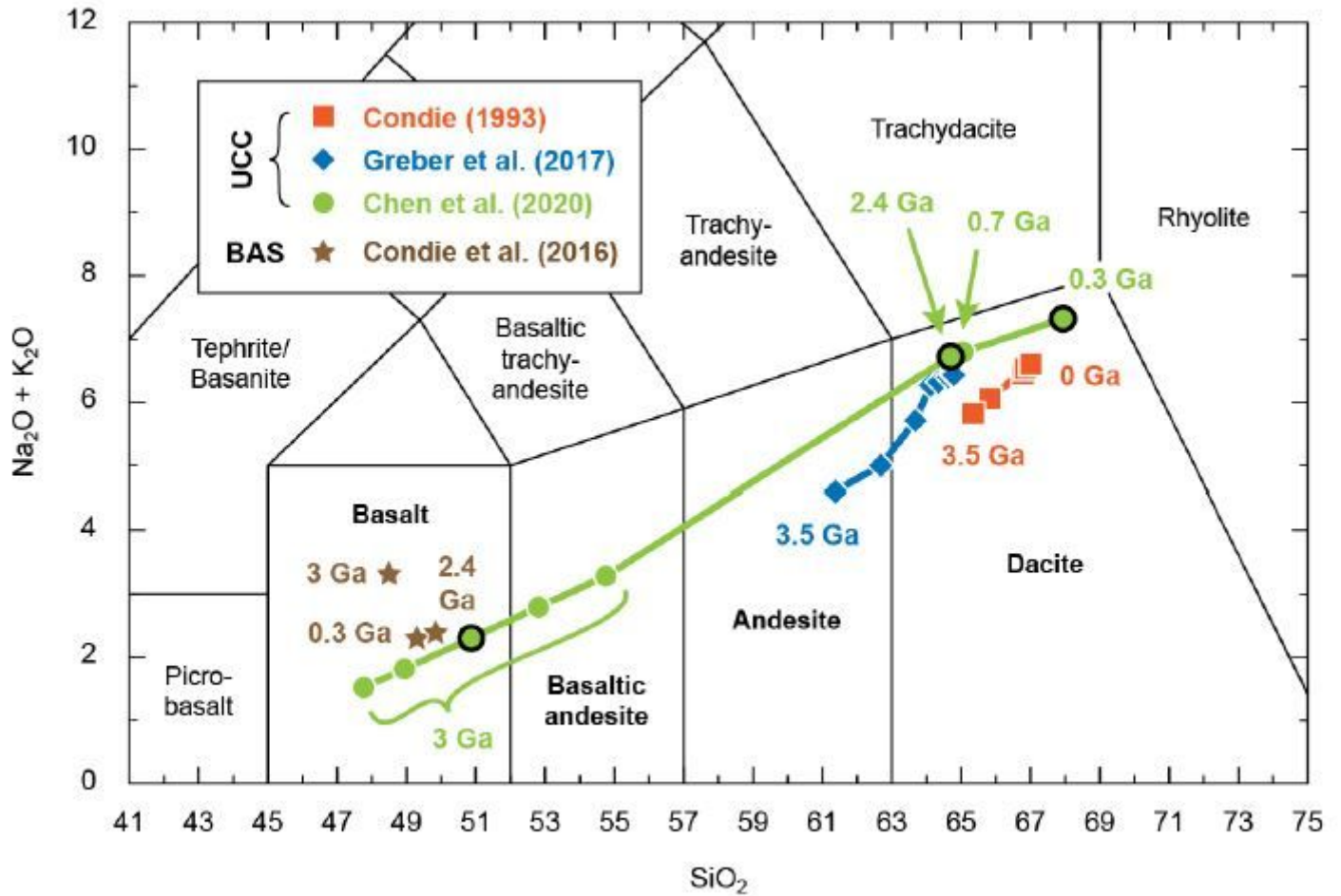
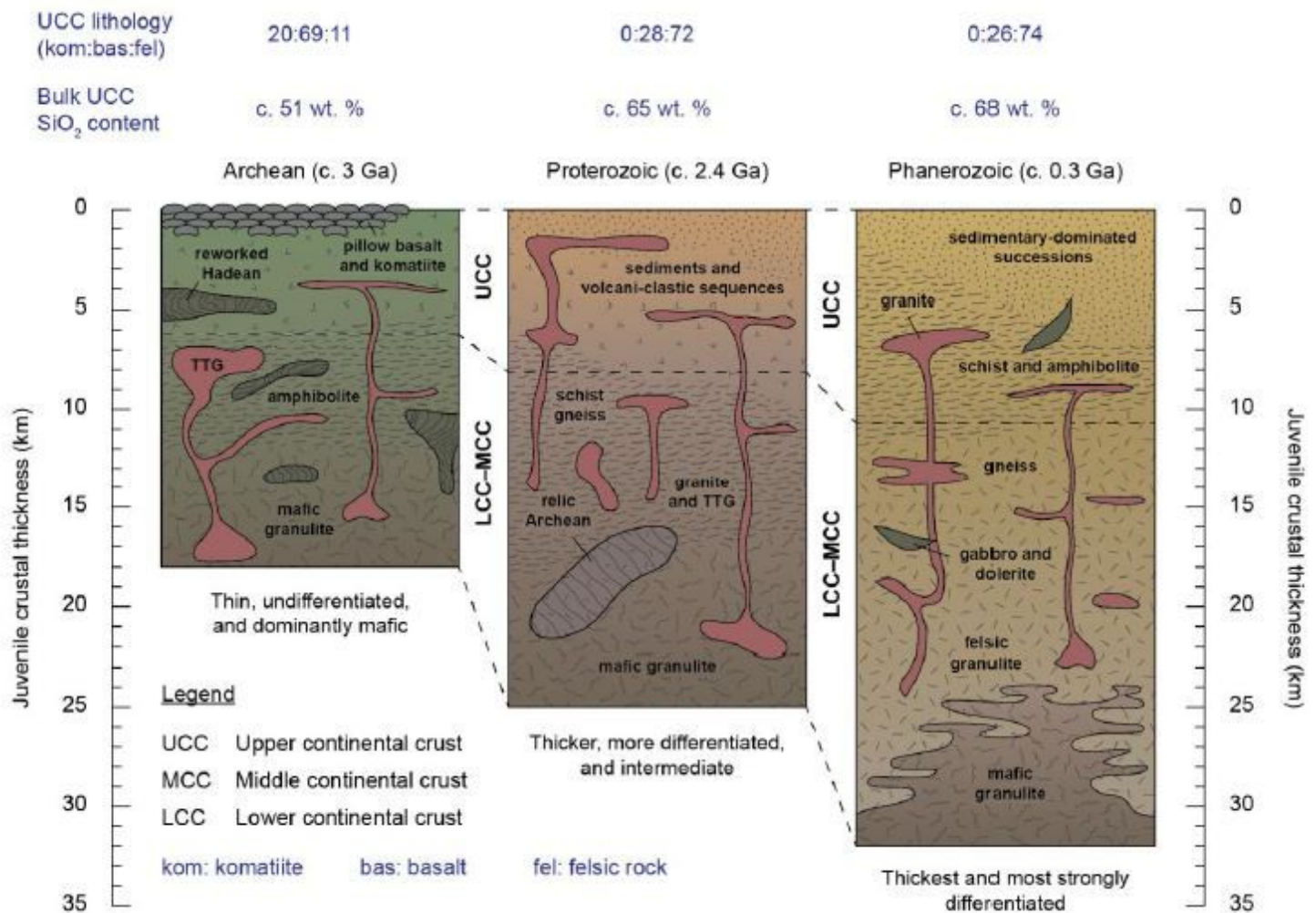


Figure 1

Total alkali-silica diagram showing bulk compositions of crustal lithologies considered in this study. Representative compositions are shown for upper continental crust (UCC) and continental basalt (BAS) of Archean (3 Ga), Proterozoic (2.4 Ga), and Phanerozoic (0.3 Ga) age.



**Figure 2**

Secular change in continental crust structure, lithology, and composition through time. Secular changes in reconstructed composition, thickness, and petrological components are emphasised. Phanerozoic and Proterozoic profiles modified with permission after ref. 13.

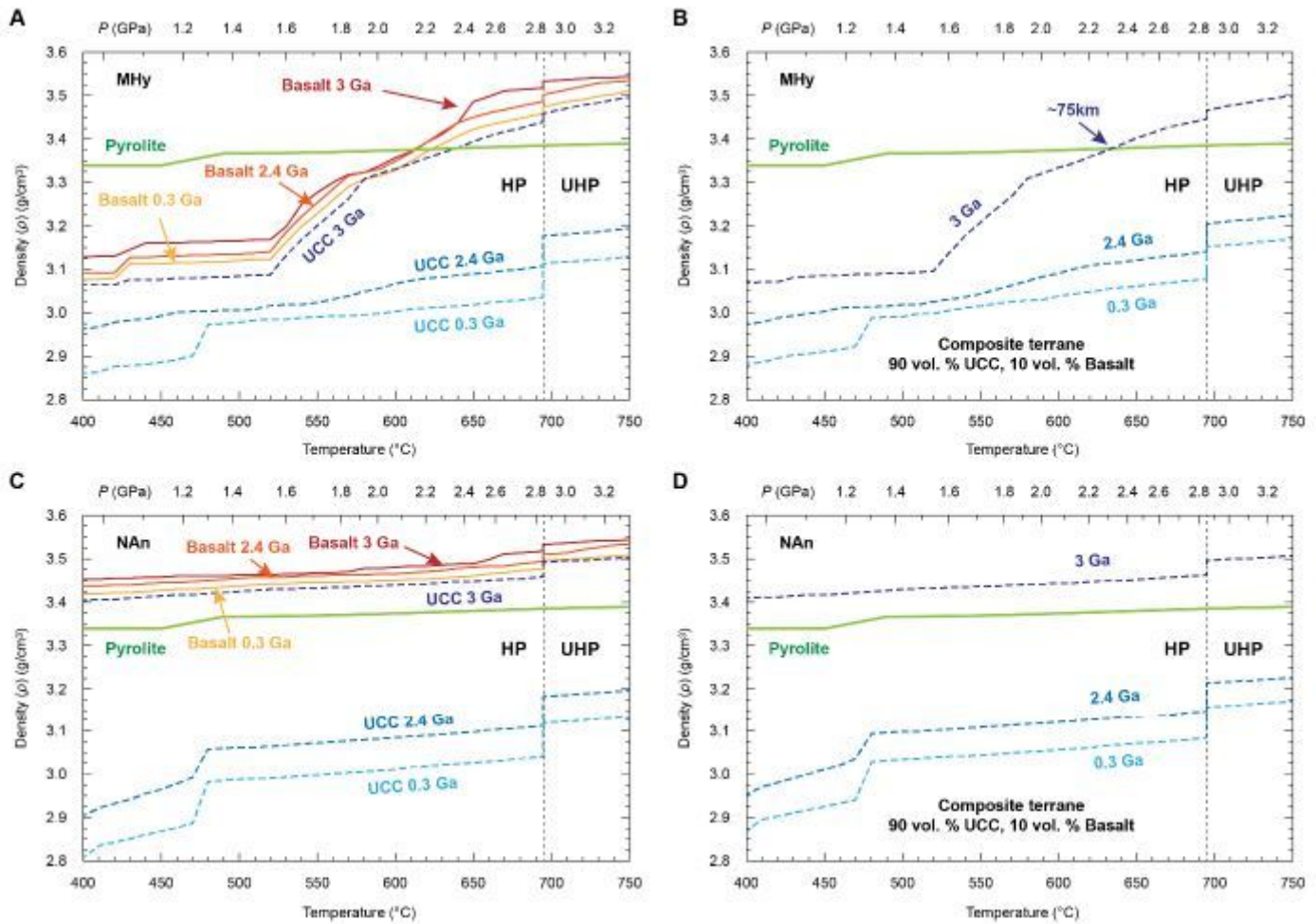


**Figure 3**

Calculated density profiles along a typical subduction zone geotherm. Values for (A) minimally hydrated (MHy) continental crust and basalt and a (B) composite terrane with volume proportions of these lithologies in the ratio 90:10, respectively, during metamorphism along an average subduction zone pressure–temperature (P–T) path. (C–D) As for parts A–B, but 494 for nominally anhydrous (NAn) equivalents of each lithology.

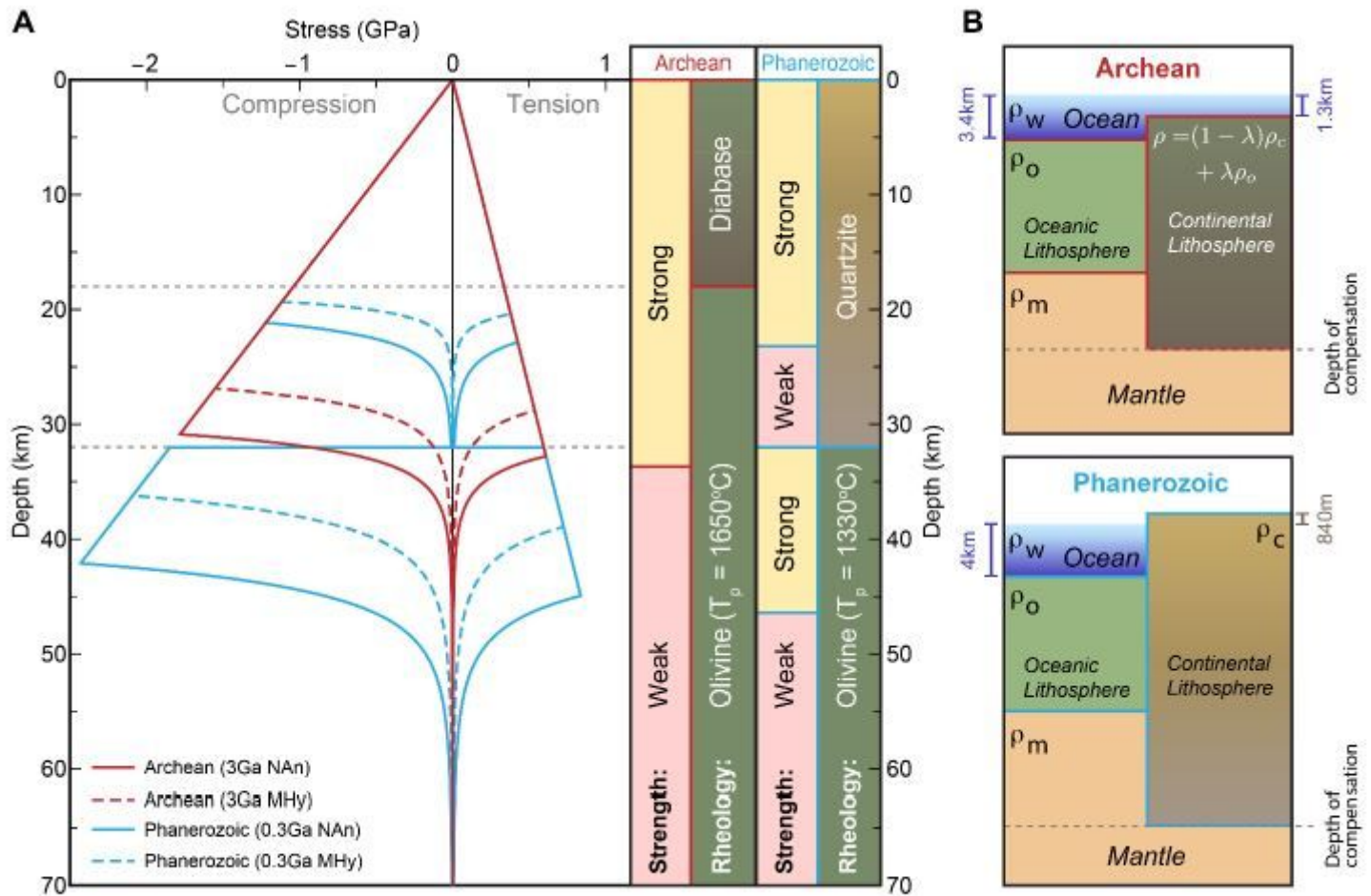


**Figure 4**

Rheological and hypsometric implications of changes in continental crust composition. (A) Yield strength envelope (YSE) for Archean (red) and Phanerozoic (blue) lithosphere under nominally anhydrous (NAn, solid lines) and minimally hydrated (MHy, dashed lines) conditions. The relative strength of the lithosphere and rheology employed to generate the 501 YSE are shown for reference. TP = mantle potential temperature. (B) Schematic cross sections 502 through Archean and Phanerozoic lithosphere demonstrating changes in hypsometry under isostatic equilibrium.  $p$  = density;  $w$  = water;  $o$  = oceanic lithosphere;  $m$  = asthenospheric mantle;  $c$  = Phanerozoic continental lithosphere;  $\lambda$  = basalt fraction in Archean continental crust.

## Supplementary Files

This is a list of supplementary files associated with this preprint. Click to download.

- [Supplementaryinformation.pdf](#)
- [Supplementaryinformation.pdf](#)